

SDSS-IV MaNGA: Stellar population correlates with stellar root-mean-square velocity V_{rms} gradients or total-density-profile slopes at fixed effective velocity dispersion σ_e

Shengdong Lu^{1,2*}, Michele Cappellari³, Shude Mao^{4,1}, Junqiang Ge¹, Ran Li^{1,5}

¹National Astronomical Observatories, Chinese Academy of Sciences, 20A Datun Road, Chaoyang District, Beijing 100101, China

²University of Chinese Academy of Sciences, Beijing 100049, China

³Sub-department of Astrophysics, Department of Physics, University of Oxford, Denys Wilkinson Building, Keble Road, Oxford, OX1 3RH, UK

⁴Department of Astronomy and Tsinghua Center for Astrophysics, Tsinghua University, Beijing 100084, China

⁵School of Astronomy and Space Science, University of Chinese Academy of Science, Beijing 100049, China

Accepted ***, Received ***, in original form ***

ABSTRACT

Galaxy properties are known to correlate most tightly with the galaxy effective stellar velocity dispersion σ_e . Here we look for *additional* trends at fixed σ_e using 1339 galaxies ($M_* \gtrsim 6 \times 10^9 M_\odot$) with different morphologies in the MaNGA (DR14) sample with integral-field spectroscopy data. We focus on the gradients ($\gamma_{\text{rms}} \equiv \sigma(R_e/4)/\sigma_e$) of the stellar root-mean-square velocity ($V_{\text{rms}} \equiv \sqrt{V^2 + \sigma^2}$), which we show traces the total mass-density gradient γ_{tot} derived from dynamical models and, more weakly, the bulge fraction. We confirm that γ_{rms} increases with σ_e , age and metallicity. We additionally find that these correlations still exist at fixed σ_e , where galaxies with larger γ_{rms} are found to be older and more metal-rich. It means that mass-density gradients contain information of the stellar population which is not fully accounted for by σ_e . This result puts an extra constraint on our understanding of galaxy quenching. We compare our results with galaxies in the IllustrisTNG hydrodynamical simulations and find that, at fixed σ_e , similar trends exist with age, the bulge fraction, and the total mass density slope but, unlike observations, no correlation with metallicity can be detected in the simulations.

Key words: galaxies: formation – galaxy: evolution – galaxy: kinematics and dynamics – galaxies: structure

1 INTRODUCTION

Galaxy properties have already been found to strongly correlate with their morphologies. One of the quantities that are used to describe the morphology of galaxies is the bulge fraction. However, the photometric bulge+disk decomposition is a complex process, which depends on the extraction details and suffers from degeneracies (Cappellari et al. 2013b, hereafter C13b). Due to the degeneracies of projection, the intrinsic 3D stellar density cannot be uniquely recovered from the 2D images unless the galaxies are edge-on, even if we assume galaxies are axisymmetric (Rybicki 1987; Gerhard & Binney 1996; van den Bosch 1997; Magorrian et al. 1998). The fact that one cannot infer the intrinsic density of inclined galaxies implies that one cannot uniquely decompose their bulges and disks of inclined galaxies ($i < 90^\circ$) unless we know the galaxies to be accurately described by Sersic (1968) bulges and exponential disks (Freeman 1970). Cappellari et al. (2011) used the *kinematic morphology* (i.e. fast and slow rotators) to study the re-

lation between galaxy type and the environment density (i.e. the $T - \Sigma$ relation), instead of using classic morphology (i.e. lenticulars and ellipticals). It is found that the $T - \Sigma$ relation is cleaner when the kinematic morphology is adopted. It implies that combining dynamical properties may be beneficial for analyzing the structure of galaxies. In C13b, σ_e (the velocity dispersion within the half-light radius R_e) is shown to be related to the bulge fraction of galaxies (see fig. 5 of C13b).

Cappellari et al. (2006) found that the stellar mass-to-light ratio M_*/L , which is related to the stellar population, tightly correlates with σ_e rather than mass or R_e . Similarly, Graves et al. (2009) used the Fundamental Plane to conclude that no stellar population property shows any dependence on R_e at fixed σ_e . The primary role of σ_e in driving variations in both the stellar population indicators (M_*/L , colors, and line indices) and the molecular gas content was clearly demonstrated by C13b and with population models by McDermid et al. (2015) using the high-quality data from the ATLAS^{3D} survey. The latter ATLAS^{3D} works showed that all population and gas content indicators closely follow lines of constant σ_e on the mass-size plane. It indicates that σ_e , which traces

* E-mail: lushengdong@nao.cas.cn

the bulge fraction, is the main driver for the observed trends of the stellar population properties on the mass-size plane. This result is verified with a larger sample of galaxies with different morphologies from SAMI (Scott et al. 2017, 1319 galaxies) and MaNGA (Li et al. 2018, ~ 2000 galaxies).

Given that galaxy properties correlate with σ_e and that this in turn appears related to the galaxies bulge fraction, or the steepness of the total density profile, it is natural to ask whether other quantities contain extra information on the population that is not already contained in σ_e alone. More specifically, we want to see whether there is a residual correlation of stellar population properties with the root-mean-square velocity ($V_{\text{rms}} \equiv \sqrt{V^2 + \sigma^2}$, where V and σ are the mean line-of-sight velocity and dispersion) profile at fixed σ_e . In C13b, the shape of V_{rms} map is proved to have the ability to trace the bulge fraction at even low inclinations (close to face-on, $i \sim 30^\circ$, see fig. 4 of C13b). The gradient of V_{rms} (defined there as $\sigma(R_e/8)/\sigma_e$, where $\sigma(R_e/8)$ is the velocity dispersion within $R_e/8$), which is used to describe the shape of V_{rms} map, is found to have similar distribution as stellar population properties on the mass-size plane, which implies the correlations between the gradient of V_{rms} and stellar populations. However the ATLAS^{3D} sample only contains 260 galaxies and does not allow one to assess whether a residual trends exists at fixed σ_e , due to the small-numbers statistics (see Cappellari 2016 for a review).

With the advancement of the largest Integral Field Unit (IFU) survey MaNGA (Bundy et al. 2015), we are able to study the underlying relations between the kinematics and the stellar populations in detail with a sufficiently large number of galaxies with different morphologies. The goals of this paper are: (i) to investigate the correlations between the gradient of V_{rms} and galaxy properties (i.e. age, metallicity, the bulge fraction, and the steepness of total mass profile); (ii) to examine whether the correlations still exist at fixed σ_e which is never addressed before; (iii) to compare with the state-of-the-art hydrodynamical simulations, the IllustrisTNG simulations (Marinacci et al. 2018; Naiman et al. 2018; Nelson et al. 2018; Pillepich et al. 2018; Springel et al. 2018).

This paper is organized as follows. In Section 2, we describe our sample selection in MaNGA (Section 2.1) and IllustrisTNG simulations (Section 2.2). The general property of the V_{rms} gradient is presented in Section 3.1. Section 3.2 is devoted to presenting the correlations between the gradient of V_{rms} and galaxy properties. In Section 3.3, we investigate the relations between the gradient of V_{rms} and galaxy properties at fixed σ_e . Finally, we summarize our findings in Section 4.

2 DATA

2.1 MaNGA galaxies

The galaxies in this study are from the MaNGA sample released by SDSS DR14 (Abolfathi et al. 2018), which includes 2778 galaxies with different morphologies. We note here that we do not use the latest data release of MaNGA because we want our results to rely on published data (i.e. stellar population and structural properties) from other papers. The kinematical data are extracted from the IFU spectra using the MaNGA data analysis pipeline (DAP; Westfall et al. 2019) by fitting absorption lines, making use of the PPXF software (Cappellari & Emsellem 2004; Cappellari 2017) with a subset of the MILES (Sánchez-Blázquez et al. 2006; Falcón-Barroso et al. 2011) stellar library, MILES-THIN. Before fitting, the spectra are Voronoi binned (Cappellari & Copin 2003) to S/N = 10. Readers

are referred to the following papers for more details on the MaNGA instrumentation (Drory et al. 2015), observing strategy (Law et al. 2015), spectrophotometric calibration (Smee et al. 2013; Yan et al. 2016a), and survey execution and initial data quality (Yan et al. 2016b).

We exclude the galaxies which are merging or have low data quality (with fewer than 100 Voronoi bins with S/N greater than 10) from our sample. Besides, we exclude galaxies with low stellar mass ($M_* < 6 \times 10^9 M_\odot$) to achieve a comparable minimum stellar mass as in C13b. The stellar mass of MaNGA galaxies is derived from Salim et al. (2016, table 1), in which the state-of-the-art spectral energy distribution (SED) fitting of UV and optical fluxes is adopted. After excluding the galaxies described above, we have 1520 galaxies with different morphologies. We derive the stellar population properties (i.e. age and metallicity) from Li et al. (2018, see their online table A1), which are calculated as the luminosity-weighted values within an elliptical aperture of area $A = \pi R_e^2$. We use the mass-weighted total density slope (γ_{tot}) from Li et al. (2019, a subset¹ of the values for our galaxies is included in Table 1) to describe the total mass profiles of galaxies (see Li et al. 2019, eq. 2 for definition). The bulge-to-total luminosity ratio (B/T) is from Simard et al. (2011, table 1). After cross-matching these four catalogs, we have 1339 galaxies with available galaxy properties in our final sample, including 646 early-type galaxies and 693 late-type galaxies. The morphologies of galaxies are classified with the catalogue in table A1 of Li et al. (2018), which is based on the *Galaxy Zoo 1* (Lintott et al. 2008, 2011) and the Sérsic index (Sérsic 1968). The size parameters (i.e. the half-light radius R_e and the major axis of the half-light isophote R_e^{maj}) used in this work are calculated from the Multi-Gaussian Expansion (MGE) models (Emsellem et al. 1994) with the fitting algorithm and PYTHON software² by Cappellari (2002) and are scaled by a factor of 1.35 (see fig. 7 of Cappellari et al. 2013a).

2.2 Galaxies in hydrodynamical simulations

For comparison, we also select a sample of simulated galaxies with the same stellar mass range ($M_* > 6 \times 10^9 M_\odot$) at $z = 0$ from the state-of-the-art magneto-hydrodynamic cosmological galaxy formation simulations, the IllustrisTNG simulations³ (TNG hereafter; Marinacci et al. 2018; Naiman et al. 2018; Nelson et al. 2018; Pillepich et al. 2018; Springel et al. 2018). In this work, we use its full-physics version with a cubic box of 110.7 kpc side length (TNG100) which has been made publicly available (Nelson et al. 2019). The mass resolutions of the TNG100-full physics version for baryonic and dark matter are $m_{\text{baryon}} = 1.4 \times 10^6 M_\odot$ and $m_{\text{DM}} = 7.5 \times 10^6 M_\odot$, with a gravitational softening length of $\epsilon = 0.74$ kpc. Gas cells are resolved in a fully adaptive manner with a minimum softening length of 0.19 comoving kpc. All selected galaxies are central galaxies whose host dark matter subhaloes are identified by the SUBFIND algorithm (Springel et al. 2001; Dolag et al. 2009). Thus, we have 5105 simulated galaxies in our sample.

To derive galaxy properties of simulated galaxies, we first use the MGE method to fit the projected SDSS r -band (Stoughton et al. 2002) image. The age, metallicity, and σ_e of TNG galaxies are then

¹ Readers need to cite Li et al. (2019) if they want to use the total density slope in this work.

² The software is available from <http://www-astro.physics.ox.ac.uk/~mxc/software>

³ <http://www.tng-project.org>

calculated as luminosity-weighted values within an elliptical aperture, the same as for MaNGA galaxies. The bulge-to-total ratio of TNG galaxies is from Xu et al. (2019). We refer the readers to Xu et al. (2017) for detailed descriptions of galaxy property extraction. The total mass density slopes of TNG galaxies are from Li et al. (2019). All these related properties of TNG galaxies can be derived from the journal website and readers are required to cite Xu et al. (2019) if they need to use the bulge fraction in this work.

We note here that we want to make an impeccable comparison with the IllustrisTNG simulations, and as a result, we exclude the galaxies with low stellar mass ($M_* < 6 \times 10^9 M_\odot$) in MaNGA. This mass limit roughly matches the mass cutoff of the IllustrisTNG simulations ($\sim 5 \times 10^9 M_\odot$, below which the galaxies may not be sufficiently resolved). We have also examined our results with all qualified galaxies in MaNGA regardless of their stellar masses and find our results remain unchanged.

3 RESULTS

In this section, we first present the distribution of the gradient of V_{rms} in Section 3.1. Then we show the relations between the gradient of V_{rms} and galaxy properties (i.e. B/T, γ_{tot} , log Age, and [Z/H]) in Section 3.2. Section 3.3 is devoted to presenting the relation between the gradient of V_{rms} and galaxy properties at fixed σ_e .

3.1 The gradient of V_{rms}

Similarly to C13b, we define the gradient of V_{rms} as:

$$\gamma_{\text{rms}} \equiv \frac{\sigma(R_e/4)}{\sigma_e}, \quad (1)$$

where $\sigma(R_e/4)$ and σ_e are the luminosity-weighted V_{rms} within a circular aperture of radius $R = R_e/4$ and an elliptical aperture of area $A = \pi R_e^2$, respectively (see the definition in Li et al. 2018, eq. 2). The $\sigma(R_e/4)$ and σ_e so defined agree closely with the velocity dispersions measured from a single fit to the spectrum inside the same apertures in C13b (Li et al. 2018). If a galaxy has $\gamma_{\text{rms}} > 1$, that means there is a decrease of V_{rms} from the inner to the outer region of this galaxy. We note here that due to the limitation of spatial resolution in MaNGA, we use a larger ($R_e/4$ instead of $R_e/8$) aperture for the central velocity dispersion compared to that in C13b. Part of the results are listed in Table 1. For simulated galaxies, $\langle v_{\text{los}}^2 \rangle^{1/2}$ is used to approximate the V_{rms} .

Due to the effect of seeing, we have tried to only use galaxies with $R_e/4 > 1.5''$, where $1.5''$ is the typical value of seeing in MaNGA (see Bundy et al. 2015 for more information of technical details of MaNGA), which constitute about half of our current sample (red circles with green dots in the center in Fig. 2 and Fig. 3). Our main results are found to be unchanged with only large galaxies. Besides, we have also tried to use the linear slopes of log V_{rms} profiles (log V_{rms} versus log R) to describe the gradient of V_{rms} . We first divide the galaxies into several elliptical annuli from $R_e/8$ to R_e , with the global ellipticity measured around $1R_e$. Then we calculate the median value of log V_{rms} in each annulus and perform a linear fit to get the linear slopes. We find that our main results remain unchanged when the new gradient is adopted.

We show the distribution of γ_{rms} ($\equiv \sigma(R_e/4)/\sigma_e$) on the $R_e^{\text{maj}}-M_{1/2}$ plane (the ‘mass-size plane’) in Fig. 1, where $M_{1/2}$ is the enclosed total mass within a spherical aperture of the three-dimensional half-light radius. The $M_{1/2}$ here is from Li et al. (2018)

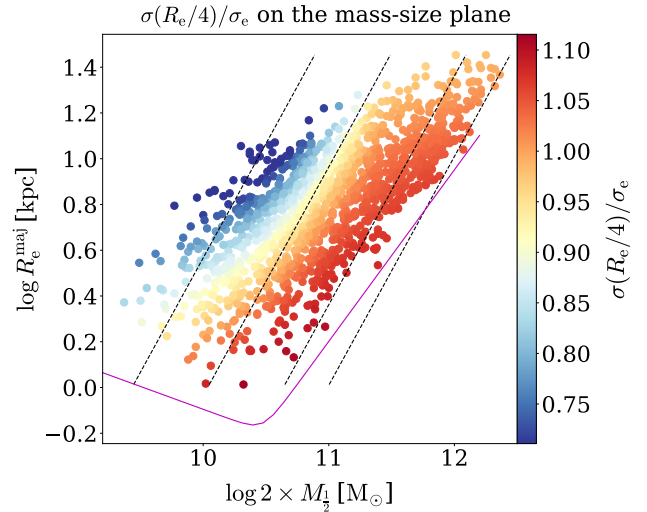


Figure 1. The distribution of MaNGA galaxies on the mass-size plane (R_e^{maj} vs. $M_{1/2}$), color-coded by the V_{rms} gradient $\gamma_{\text{rms}} (\equiv \sigma(R_e/4)/\sigma_e)$. The black dashed lines are the lines of constant σ_e : 50, 100, 200, and 300 km s^{-1} . The magenta curve is the zone of exclusion defined in C13b.

which is derived using the Jeans anisotropic model (JAM) (Cappellari 2008). Before plotting, we make use of the PYTHON implementation⁴ (see details in C13b) of the two-dimensional Locally Weighted Regression (LOESS) (Cleveland & Devlin 1988) method to obtain smoothed distribution of γ_{rms} . As can be seen, the gradient of V_{rms} varies systematically roughly along the σ_e direction, which is consistent with the result in C13b (the top panel of their fig. 6) in which $\sigma(R_e/8)/\sigma_e$ is used.

To better illustrate the correlation between γ_{rms} and σ_e , we present Fig. 2. As shown in the figure, γ_{rms} of MaNGA galaxies increases with σ_e from $\gamma_{\text{rms}} < 1$ (at low σ_e) to $\gamma_{\text{rms}} > 1$ (at high σ_e). The transition point $\gamma_{\text{rms}} = 1$, which corresponds to a flat V_{rms} profile, is at $\log \sigma_e \approx 2.1$. For $\log \sigma_e \gtrsim 2.1$, the trend becomes flatter and γ_{rms} stays at ~ 1.05 , indicating a mild decrease of V_{rms} from the central region of galaxies to the outer part. As demonstrated in C13b (fig. 5), galaxies with $\log \sigma_e \approx 2.0$ have V_{rms} maps in butterfly-like shapes with small bulges in the center, after which the peak of V_{rms} in the center gets stronger, indicating a rising bulge fraction. It implies that the relation between the gradient of V_{rms} and the bulge fraction saturates when this is larger than a threshold. In the idealized case in which the bulge and disk have fixed parametrization (e.g. exponential and Sersic profiles), this can be qualitatively understood as due to the fact that, when the bulge dominates, the V_{rms} gradient must converge to that of the bulge alone. This is illustrated in Fig. 3, in which γ_{rms} increases with B/T and levels off when $B/T \gtrsim 0.5$ (see Section 3.2 for a detailed description). This trend in γ_{rms} with σ_e is similar with the trend in total density slope γ_{tot} found by Poci et al. (2017) and Li et al. (2019), which also shows a near constant trend above $\log \sigma_e \approx 2.1$ and a break, and an increase in γ_{tot} , below that transition value (see fig. 1 of Li et al. 2019). The key difference is that γ_{rms} is a purely empirical quantity, which does not involve dynamical models. As a comparison, however, TNG galaxies show a decreasing trend at

⁴ The software is available from <https://pypi.org/project/loess/>

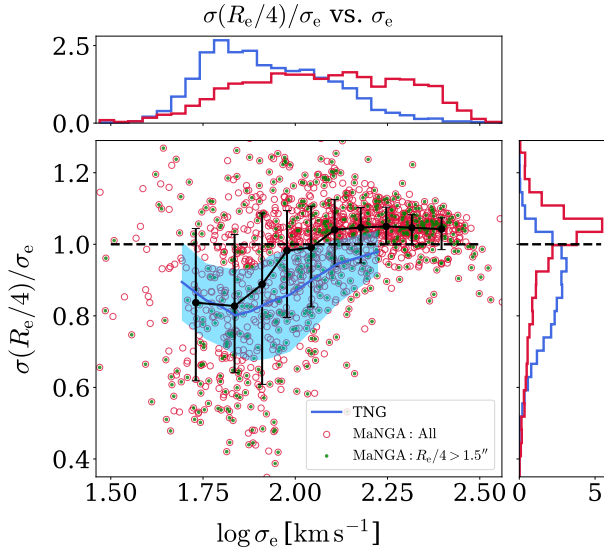


Figure 2. The relation between the V_{rms} gradient γ_{rms} and σ_e . The red circles are MaNGA galaxies and the circles with green dots in the center are the galaxies with $R_e/4 > 1.5''$, where $1.5''$ is the typical value of seeing in MaNGA. The black dots represent the median values of γ_{rms} in each V_{rms} bin, with error bars indicating the 1σ range. TNG galaxies are shown by the median profile (blue lines) with a shaded region indicating the 1σ range. The black dashed line represents $\gamma_{\text{rms}} = 1$, below which an increase of V_{rms} exists in galaxies. The histograms are the distributions of γ_{rms} and $\log \sigma_e$ for MaNGA (red) and TNG (blue) galaxies.

low σ_e end and do not show a flat tail at high σ_e end. Besides, most ($\sim 86\%$) TNG galaxies have $\gamma_{\text{rms}} < 1$, relative to 44% in MaNGA, and σ_e of TNG galaxies is typically lower than MaNGA galaxies. This may be due to the overly-strong AGN feedback (typically the isotropic black hole kinetic winds in the AGN quiescent phase) in IllustrisTNG for puffing up the galaxies (Wang et al. 2019, 2020; Lu et al. 2020).

3.2 γ_{rms} vs. galaxy properties

To investigate the relation between the V_{rms} gradient and galaxy properties (i.e. the stellar age, metallicity, the total density slope, and the bulge fraction), we present Fig. 3. As can be seen, γ_{rms} of MaNGA galaxies increases with $\log \text{Age}$ and $[Z/H]$, indicating that older and more metal-rich galaxies are more likely to have flatter or even declining V_{rms} profiles. For TNG galaxies, γ_{rms} shows a shallower correlation with $\log \text{Age}$, while it does not show an obvious correlation with $[Z/H]$. We note here that TNG lacks galaxies with low metallicity which results in the narrower range of metallicity.

For structural parameters, γ_{rms} gets higher when the bulge increases below $B/T \sim 0.5$ and keeps nearly constant at the large B/T end. It means the gradient cannot trace the bulge fraction of bulge-dominated galaxies (see also Section 3.1). For the total density slope γ_{tot} , which is defined as (Dutton & Treu 2014, eq. 1):

$$\gamma_{\text{tot}} \equiv -\frac{1}{M(R_e)} \int_0^{R_e} 4\pi r^2 \rho(r) \frac{d \log \rho}{d \log r} dr = 3 - \frac{4\pi R_e^3 \rho(R_e)}{M(R_e)}, \quad (2)$$

where $\rho(r)$ is total mass density of the galaxy and $M(R)$ is the total mass enclosed in a sphere with radius R (Li et al. 2019), the gradient of V_{rms} rises across the whole range of γ_{tot} . It means that the

MaNGA ID	$\log R_e$ [arcsec]	$\log R_e^{\text{maj}}$ [arcsec]	$\log \sigma(R_e/4)$ [km s $^{-1}$]	$\log \sigma_e$ [km s $^{-1}$]	γ_{rms}	γ_{tot}
1-24295	0.85	0.85	2.18	2.16	1.05	1.95
1-260743	0.78	0.79	2.42	2.42	1.01	2.06
1-115128	0.90	1.07	1.94	1.97	0.93	1.83
1-258820	1.11	1.25	1.63	1.87	0.59	1.14
1-251662	0.76	0.78	2.04	1.98	1.13	1.78
1-637825	1.05	1.14	1.82	1.92	0.80	1.62
1-23877	1.02	1.31	2.00	2.09	0.82	1.60
1-109521	0.85	0.91	2.29	2.28	1.02	2.02
1-321967	0.39	0.45	1.88	1.88	1.00	1.74
1-147685	0.88	1.28	1.58	1.95	0.42	0.73
1-547185	0.93	0.99	1.82	1.83	0.96	1.84
1-38550	1.15	1.21	1.83	1.84	0.99	1.53
1-351790	0.62	0.73	1.63	1.66	0.94	1.50
1-258315	0.85	0.89	1.84	1.87	0.94	1.71
1-95770	0.85	0.95	1.82	1.87	0.88	0.98
1-22347	0.46	0.49	1.99	1.98	1.01	1.89
1-135091	0.87	0.94	2.23	2.22	1.02	2.05
1-260541	0.89	0.90	2.44	2.39	1.10	2.10
1-93908	0.85	0.91	2.37	2.33	1.11	2.35
1-275354	0.93	1.04	1.74	1.81	0.86	1.57
1-339116	0.67	0.81	1.68	1.81	0.74	1.30
1-167392	0.51	0.64	1.64	1.79	0.70	0.49
1-174036	0.78	0.82	2.35	2.37	0.95	1.80
1-55552	0.76	0.81	2.31	2.27	1.07	2.18
1-24476	0.96	1.05	2.10	2.08	1.05	2.01
1-545674	1.27	1.43	1.65	1.75	0.79	0.64
1-251278	0.66	0.70	2.39	2.35	1.08	2.20
1-594505	0.93	0.93	2.26	2.23	1.08	2.37
1-167334	0.60	0.68	2.01	2.00	1.03	2.39
1-217557	0.53	0.58	2.11	2.08	1.07	2.52
1-245908	0.57	0.68	1.96	1.95	1.02	1.96
1-44047	0.32	0.42	2.08	2.11	0.94	1.80
1-210667	1.12	1.25	1.73	1.76	0.93	1.28
1-73638	0.87	1.04	2.24	2.28	0.90	1.88
1-256465	0.61	0.66	2.30	2.28	1.04	2.42

Table 1. MaNGA ID, half-light radius $\log R_e$, major axis of the half-light isophote $\log R_e^{\text{maj}}$, luminosity-weighted velocity dispersion within two apertures (a circular aperture with radius $R_e/4$ and an elliptical aperture of area $A = \pi R_e^2$), the gradient of V_{rms} ($\gamma_{\text{rms}} \equiv \sigma(R_e/4)/\sigma_e$), and the total density slope γ_{tot} (from Li et al. 2019) for part of our sample. Please see the complete table on the journal website.

steeper the mass profile, the more likely the V_{rms} profile to be flat or even declining. γ_{rms} of galaxies which are isothermal ($\gamma_{\text{tot}} = 2$) is ~ 1 , indicating that flat V_{rms} profiles are existent in these galaxies. A purely isothermal spherical isotropic galaxy has constant V_{rms} (Binney & Tremaine 2008, denoted by σ in their eq. 4.100), while in this work, the same correspondence between $\gamma_{\text{tot}} = 2$ and flat V_{rms} profile also works in our non-spherical case. By contrast, TNG galaxies show a gradually increasing but somehow shallower trend of γ_{rms} towards the high B/T and high γ_{tot} end.

3.3 Relations at fixed σ_e

The results in Section 3.2 are generally consistent with the previous studies (Cappellari et al. 2013b; Scott et al. 2017; Li et al. 2018), in which stellar age, metallicity, and the gradient of V_{rms} are found to have similar distributions on the mass-size plane, indicating a correlation among them. However, it is still unclear whether

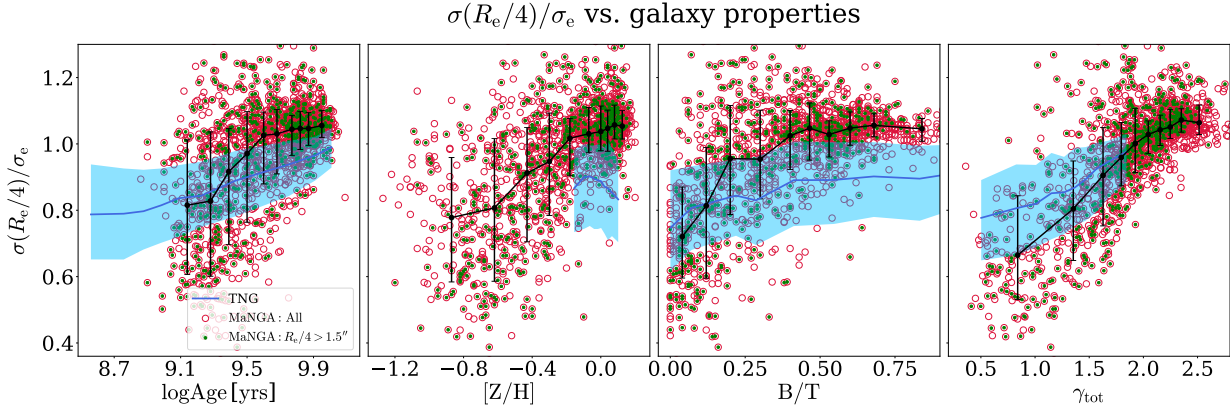


Figure 3. The relation of γ_{rms} vs. log Age, $[Z/H]$, B/T , and the total density slope γ_{tot} (from left to right). The bulge fraction of MaNGA galaxies is derived from Simard et al. (2011, table 1). The symbols are the same as Fig. 2.

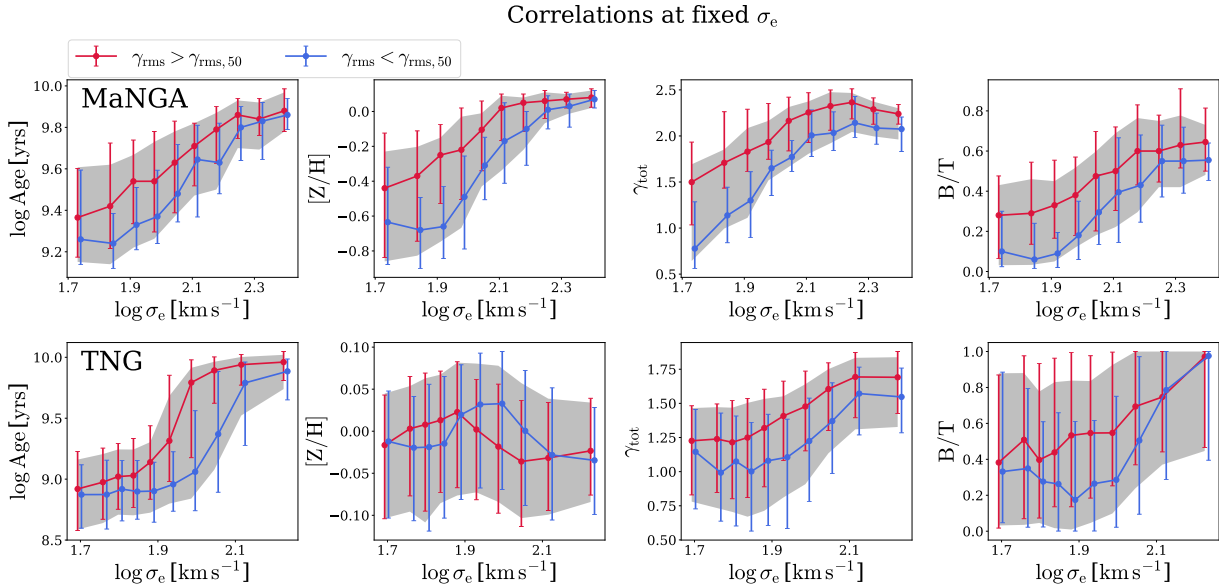


Figure 4. The trend of galaxy properties as a function of $\log \sigma_e$. Results of the stellar age, metallicity, the total density slope γ_{tot} , and the bulge fraction B/T are shown from left to right. Upper panels are for MaNGA galaxies and the bottom panels are for TNG galaxies. In each panel, galaxies in each V_{rms} bin are divided into two subgroups ($\gamma_{\text{rms}} > \gamma_{\text{rms},50}$ and $\gamma_{\text{rms}} < \gamma_{\text{rms},50}$, where $\gamma_{\text{rms},50}$ is the median value of γ_{rms} in each V_{rms} bin). Red and blue dots denote the median values of galaxy properties as shown in the Y-axis of the two subgroups ($\gamma_{\text{rms}} > \gamma_{\text{rms},50}$ and $\gamma_{\text{rms}} < \gamma_{\text{rms},50}$) with error bars indicating the 1σ range. The grey shaded region indicates the 1σ range of the correlations between galaxy properties and σ_e .

the relations are only driven by σ_e , or in other words, whether the gradient of V_{rms} still correlates with galaxy properties at fixed σ_e .

To answer this question, we first divide galaxies in our sample into 10 bins according to their $\log \sigma_e$, with the same number of galaxies in each bin. Then galaxies in each bin are further divided into two subgroups according to their V_{rms} gradient γ_{rms} ($\gamma_{\text{rms}} > \gamma_{\text{rms},50}$ and $\gamma_{\text{rms}} < \gamma_{\text{rms},50}$, where $\gamma_{\text{rms},50}$ is the median value of γ_{rms} in each V_{rms} bin). Finally, we calculate the median values of galaxy properties for galaxies of both two subgroups in each bin.

Fig. 4 shows the trends of galaxy properties as a function of $\log \sigma_e$ for both subgroups ($\gamma_{\text{rms}} > \gamma_{\text{rms},50}$ and $\gamma_{\text{rms}} < \gamma_{\text{rms},50}$). It can be clearly seen that MaNGA galaxies with different V_{rms} gradients (γ_{rms}) have obvious systematic differences between each

other. At fixed σ_e , galaxies with larger γ_{rms} (red lines) are typically older, more metal-rich, more bulge-dominated, and have steeper mass profiles. In comparison, the two subgroups of TNG galaxies also show discrepancies in the mass density slope, the bulge fraction, and the stellar age. For metallicity, however, the difference is not observed in TNG galaxies, which may imply that TNG does not well recover the relation between metallicity and other galaxy properties.

This result is also examined with only ETGs and the similar but somehow less obvious systematic differences in figures of age, metallicity, and the total density slope are still seen when late-type galaxies are excluded. We note here that the morphological classification of *Galaxy Zoo* is by design different from the classic [Hubble](#)

(1936) classification used by astronomers over the past century. In particular, the *Galaxy Zoo* classification includes most S0 galaxies in the "Spirals" galaxies category, while early-type galaxies mainly comprise Ellipticals, without photometric evidence for stellar disks. Thus, the fact that the systematic differences are less obvious when using only ETGs is expected because the removal of spirals and S0 tends to eliminate most of the age and metallicity differences in the sample. The figure of bulge fraction, however, does not show difference in the two subgroups ($\gamma_{\text{rms}} > \gamma_{\text{rms},50}$ and $\gamma_{\text{rms}} < \gamma_{\text{rms},50}$) when only ETGs are used.

The results seen from Fig. 4 indicate that the relations between σ_e and galaxy properties are not only driven by σ_e , but also by the gradient of V_{rms} . The fact that the gradient of V_{rms} contains information of both stellar populations and structural properties of galaxies, which are not fully accounted for by σ_e , is never addressed before.

4 CONCLUSION AND DISCUSSION

In this work, we study the relations between the gradient of V_{rms} ($\equiv \sqrt{V^2 + \sigma^2}$) and galaxies properties (i.e. the mass-weighted total density slope γ_{tot} , the bulge fraction B/T, galaxy age log Age, and metallicity [Z/H]) with 1339 galaxies from the MaNGA sample released by SDSS DR14, and make a comparison with the hydrodynamical simulations, the IllustrisTNG (TNG) simulations.

We employ $\gamma_{\text{rms}} (\equiv \sigma(R_e/4)/\sigma_e)$ to represent the gradient of V_{rms} and find that γ_{rms} changes systematically on the mass-size plane roughly along the direction of σ_e , consistent with C13b. Besides, γ_{rms} increases with log σ_e below log $\sigma_e \approx 2.1$. At high σ_e end, the V_{rms} gradient keeps nearly unchanged at $\gamma_{\text{rms}} \approx 1.05$, indicating a saturation in the V_{rms} slope for bulge-dominated galaxies (B/T $\gtrsim 0.5$). Most galaxies ($\sim 86\%$) in TNG appear to have $\gamma_{\text{rms}} < 1$, which means a decreasing trend of V_{rms} from inner to outer regions in galaxies, relative to 44% in MaNGA. It may be due to the overly-strong AGN feedback in TNG (Wang et al. 2019, 2020; Lu et al. 2020).

We find that V_{rms} gradients γ_{rms} are closely related (in a non-linear way) to both the total mass density gradients γ_{tot} and, more weakly, to the bulge fraction B/T, which is a more uncertain quantity. We confirm the clear trends of γ_{rms} with σ_e , age and metallicity (e.g. fig. 22 in the review by Cappellari 2016). The correlation of γ_{rms} with age is more shallow in TNG than in the observations and our clear empirical correlation of γ_{rms} with [Z/H] is completely absent in TNG.

The main goal of this paper is to look for trends in galaxy properties at fixed σ_e , which were impossible to investigate from smaller samples than MaNGA. We found that at fixed σ_e the stellar population clearly depends on the density gradients as here quantified by γ_{rms} . In particular, at fixed σ_e , galaxies with larger γ_{rms} are still older and more metal-rich. It means that both stellar populations and structural properties of galaxies are not fully accounted for by σ_e and the gradient of V_{rms} also contains these information. In TNG, galaxy age, γ_{tot} , and B/T show qualitatively similar trends as we derive from the MaNGA data, but the trends at fixed σ_e of γ_{rms} with [Z/H], which are clearly visible in MaNGA, are again completely absent in the simulations. It implies that the relation between metallicity and stellar age (and also other galaxy properties) seen in observations is not met in TNG.

This new empirical evidence that galaxy properties still correlate with the V_{rms} gradient γ_{rms} at fixed σ_e provides an extra constraint on our understanding of galaxy quenching. In the current

state-of-the-art simulations (e.g. the IllustrisTNG simulations), the relations between galaxy properties and γ_{rms} are not well recovered, which shows the power of investigating this extra quantity – it can be used to validate the simulations in terms of the relations between stellar population and dynamical properties of galaxies.

ACKNOWLEDGEMENTS

This work is partly supported by the National Key Basic Research and Development Program of China (No. 2018YFA0404501 to SM), by the National Natural Science Foundation of China (Grant Nos. 11821303, 11761131004 and 11761141012 to SM, 11903046 to JG), and by the Beijing Municipal Natural Science Foundation (No. 1204038 to JG). RL is supported by National Natural Science Foundation of China (Nos. 11773032 and 118513) and the NAOC Nebula Talents Program.

REFERENCES

- Abolfathi B., et al., 2018, *ApJS*, **235**, 42
- Binney J., Tremaine S., 2008, *Galactic Dynamics: Second Edition*. Princeton University Press, Princeton, NJ
- Bundy K., et al., 2015, *ApJ*, **798**, 7
- Cappellari M., 2002, *MNRAS*, **333**, 400
- Cappellari M., 2008, *MNRAS*, **390**, 71
- Cappellari M., 2016, *ARA&A*, **54**, 597
- Cappellari M., 2017, *MNRAS*, **466**, 798
- Cappellari M., Copin Y., 2003, *MNRAS*, **342**, 345
- Cappellari M., Emsellem E., 2004, *PASP*, **116**, 138
- Cappellari M., et al., 2006, *MNRAS*, **366**, 1126
- Cappellari M., et al., 2011, *MNRAS*, **416**, 1680
- Cappellari M., et al., 2013a, *MNRAS*, **432**, 1709
- Cappellari M., et al., 2013b, *MNRAS*, **432**, 1862
- Cleveland W. S., Devlin S. J., 1988, *Journal of the American Statistical Association*, **83**, 596
- Dolag K., Borgani S., Murante G., Springel V., 2009, *MNRAS*, **399**, 497
- Drory N., et al., 2015, *AJ*, **149**, 77
- Dutton A. A., Treu T., 2014, *MNRAS*, **438**, 3594
- Emsellem E., Monnet G., Bacon R., 1994, *A&A*, **285**, 723
- Falcón-Barroso J., Sánchez-Blázquez P., Vazdekis A., Ricciardelli E., Cardiel N., Cenarro A. J., Gorgas J., Peletier R. F., 2011, *A&A*, **532**, A95
- Freeman K. C., 1970, *ApJ*, **160**, 811
- Gerhard O. E., Binney J. J., 1996, *MNRAS*, **279**, 993
- Graves G. J., Faber S. M., Schiavone R. P., 2009, *ApJ*, **698**, 1590
- Hubble E. P., 1936, *Realm of the Nebulae*
- Law D. R., et al., 2015, *AJ*, **150**, 19
- Li H., et al., 2018, *MNRAS*, **476**, 1765
- Li R., et al., 2019, *MNRAS*, **490**, 2124
- Lintott C. J., et al., 2008, *MNRAS*, **389**, 1179
- Lintott C., et al., 2011, *MNRAS*, **410**, 166
- Lu S., et al., 2020, *MNRAS*, **492**, 5930
- Magorrian J., et al., 1998, *AJ*, **115**, 2285
- Marinacci F., et al., 2018, *MNRAS*, **480**, 5113
- McDermid R. M., et al., 2015, *MNRAS*, **448**, 3484
- Naiman J. P., et al., 2018, *MNRAS*, **477**, 1206
- Nelson D., et al., 2018, *MNRAS*, **475**, 624
- Nelson D., et al., 2019, *Computational Astrophysics and Cosmology*, **6**, 2
- Pillepich A., et al., 2018, *MNRAS*, **475**, 648
- Poci A., Cappellari M., McDermid R. M., 2017, *MNRAS*, **467**, 1397
- Rybicki G. B., 1987, in de Zeeuw P. T., ed., *IAU Symposium Vol. 127, Structure and Dynamics of Elliptical Galaxies*. p. 397, doi:10.1007/978-94-009-3971-4_41
- Salim S., et al., 2016, *ApJS*, **227**, 2

- Sánchez-Blázquez P., et al., 2006, [MNRAS](#), **371**, 703
- Scott N., et al., 2017, [MNRAS](#), **472**, 2833
- Sersic J. L., 1968, Atlas de Galaxias Australes
- Simard L., Mendel J. T., Patton D. R., Ellison S. L., McConnell A. W., 2011, [ApJS](#), **196**, 11
- Smee S. A., et al., 2013, [AJ](#), **146**, 32
- Springel V., White S. D. M., Tormen G., Kauffmann G., 2001, [MNRAS](#), **328**, 726
- Springel V., et al., 2018, [MNRAS](#), **475**, 676
- Stoughton C., et al., 2002, [AJ](#), **123**, 485
- Wang Y., et al., 2019, [MNRAS](#), **490**, 5722
- Wang Y., et al., 2020, [MNRAS](#), **491**, 5188
- Westfall K. B., et al., 2019, [AJ](#), **158**, 231
- Xu D., Springel V., Sluse D., Schneider P., Sonnenfeld A., Nelson D., Vogelsberger M., Hernquist L., 2017, [MNRAS](#), **469**, 1824
- Xu D., et al., 2019, [MNRAS](#), **489**, 842
- Yan R., et al., 2016a, [AJ](#), **151**, 8
- Yan R., et al., 2016b, [AJ](#), **152**, 197
- van den Bosch F. C., 1997, [MNRAS](#), **287**, 543